Published in final edited form as:

Cancer Res. 2018 August 01; 78(15): 4282–4291. doi:10.1158/0008-5472.CAN-17-3821.

Radiotherapy and CD40 activation separately augment immunity to checkpoint blockade in cancer

Andrew J. Rech[1], **Hannah Dada**[2], **Jonathan J. Kotzin**[3,4], **Jorge Henao-Mejia**[3,4,6], **Andy J. Minn**[1,4,5,7], **Christina Twyman-Saint Victor**[2,5,*], and **Robert H. Vonderheide**[1,2,4,7,*]

[1]Abramson Family Cancer Research Institute, Perelman School of Medicine, University of Pennsylvania, 3400 Civic Center Blvd., Philadelphia, PA 19104, USA

[2]Department of Medicine, Perelman School of Medicine, University of Pennsylvania, 3400 Civic Center Blvd., Philadelphia, PA 19104, USA

[3]Department of Pathology and Laboratory Medicine, Perelman School of Medicine, University of Pennsylvania, 3400 Civic Center Blvd., Philadelphia, PA 19104, USA

[4]Institute for Immunology, Perelman School of Medicine, University of Pennsylvania, 3400 Civic Center Blvd., Philadelphia, PA 19104, USA

[5]Department of Radiation Oncology, Perelman School of Medicine, University of Pennsylvania, 3400 Civic Center Blvd., Philadelphia, PA 19104, USA

[6]Division of Transplant Immunology, The Children's Hospital of Philadelphia, Philadelphia, Pennsylvania 19104, USA

[7]Abramson Cancer Center, University of Pennsylvania, 3400 Civic Center Blvd., Philadelphia, PA 19104, USA

Abstract

Immunotherapy in pancreatic ductal adenocarcinoma (PDA) remains a difficult clinical problem despite success in other disease types with immune checkpoint blockade (ICB) and chimeric antigen receptor T cell therapy. Mechanisms driving immunosuppression and poor T cell infiltration in PDA are incompletely understood. Here we use genetically engineered mouse models of PDA that recapitulate hallmarks of human disease to demonstrate that CD40 pathway activation is required for clinical response to radiotherapy (RT) and ICB with αCTLA-4 and αPD-1. The combination of an agonist αCD40 antibody, RT, and dual ICB eradicated irradiated and unirradiated (*i.e.* abscopal) tumors, generating long-term immunity. Response required T cells and also short-lived myeloid cells and was dependent on the long non-coding RNA myeloid regulator *Morrbid*. Using unbiased random forest machine learning, we built unique, contextual signatures for each therapeutic component, revealing that (i) RT triggers an early proinflammatory stimulus, ablating existing intratumoral T cells and upregulating MHC class I and CD86 on antigen presenting cells, (ii) αCD40 causes a systemic and intratumoral reorganization of the

Corresponding Author: Robert H. Vonderheide (rhv@upenn.edu), Corresponding Author mailing address: 12 South Pavilion, University of Pennsylvania, 3400 Civic Center Blvd, Philadelphia, PA 19104.
*Contributed equally to this work.

Conflict of Interest: The authors declare no potential conflicts of interest

myeloid compartment, and (iii) ICB increases intratumoral T cell infiltration and improves the CD8 T cell:regulatory T cell ratio. Thus, αCD40 and RT non-redundantly augment anti-tumor immunity in PDA, which is otherwise refractory to ICB, providing a clear rationale for clinical evaluation.

Keywords

anti-cytotoxic T lymphocyte antigen-4; anti-programmed cell death protein-1; anti-CD40; immunotherapy; pancreatic cancer; radiation therapy; random forest; machine learning; combination therapy

INTRODUCTION

Despite the success of cancer immunotherapy in many disease types, pancreatic ductal adenocarcinoma (PDA) is notably unresponsive to immune checkpoint blockade (ICB) with αPD1 and/or αCTLA4 (1–4). PDA is projected to become the second leading cause of cancer-related deaths in the United States by 2030, with a five-year overall survival of less than 10% (5,6). Despite advances in cancer therapy, the overall mortality for PDA remains high, which is attributable to late diagnosis, early metastatic spread, and poor response to therapy (7–9). Thus, novel treatment strategies are needed to improve outcomes.

Unlike other cancers that are responsive to ICB (*e.g.* melanoma), the PDA tumor microenvironment harbors dense desmoplasia and an immunosuppressive infiltrate that typically excludes CD8 T cells and represents a site of acquired immune privilege (10–14). Whereas the total predicted load of classically defined neoepitopes does not correlate with cytolytic immune activity in PDA (15), the presence of “high quality” tumor neoepitopes and CD8 infiltration positively correlates with long-term survival in resectable patients (16,17). Thus, novel therapeutic strategies should be aimed at overcoming these mechanisms of resistance to promote a more favorable tumor microenvironment and anti-tumor response.

Understanding the potential of combining ICB with chemotherapy, radiotherapy, and/or immunotherapy is therefore a high priority in PDA. Radiotherapy (RT), first understood to act locally via DNA damage, is also immunomodulatory (18). Using a preclinical mouse model of metastatic melanoma, we previously demonstrated that combining RT with αPD1 and αCTLA4 ICB improved response through distinct mechanisms, and we correlated these findings in a phase I/II clinical trial (19). In PDA, we and others have demonstrated that αCD40 agonist can activate anti-tumor myeloid cells and, in combination with gemcitabine and nab-paclitaxel, αCD40 triggers T cell immunity in PDA mouse models (20–22). Thus, we hypothesized that combining RT, αCD40, and ICB would generate immunity in PDA via multiple, non-redundant cellular mechanisms.

Here, we used the genetically engineered KrasLSL^{G12D}-Trp53LSL^{R172H}-Pdx1-Cre (KPC) mouse model that recapitulates the key genetic, stromal, and immunosuppressive features of human PDA (10,23). The KPC model was used to determine the contribution to response of each therapeutic component (RT, αCD40, and αCTLA4/αPD1 ICB). Our results indicate that ICB alone is ineffective, but the addition of RT and αCD40 overrides resistance via

short-lived myeloid cells and CD4/8 T cells in a manner independent of canonical innate activation pathways. Furthermore, using unbiased machine learning to understand the immune response, we identify that each therapeutic component non-redundantly alters the tumor microenvironment.

METHODS

Cell lines and tissue culture

Mouse KPC pancreatic cancer cell line 4662 (KPC.4662) was derived from single-cell suspensions of PDA tissue from KPC mice as previously described (24), and the C57BL/6 background of KPC mice was confirmed using DartMouse (Geisel School of Medicine at Dartmouth) as previously described (21). B16-F10 was obtained from ATCC. Cell lines were determined to be pathogen free using the Infectious Microbe PCR Amplification Test and authenticated by the Research Animal Diagnostic Laboratory at the University of Missouri. Cell lines were used within 3 weeks of being thawed. KPC.4662 and B16-F10 cells were cultured at 37°C in Dulbecco's Modified Eagle Medium (DMEM) containing 10% heat inactivated fetal bovine serum (FBS, Gemini Bio), 100 U/ml penicillin, 100μg/ml streptomycin, and 2mM L-glutamine.

Mouse strains

Murine models were on the C57BL/6J background and were obtained from The Jackson Laboratory and/or bred at the University of Pennsylvania (see Supplemental Methods). Mice were 5–8 weeks old at the time of tumor injection and strains were a mixture of male and female. All mice were housed under pathogen-free conditions at the University of Pennsylvania. Animal protocols were approved by the Institute of Animal Care and Use Committee at the University of Pennsylvania.

Tumor models

KPC.4662 and B16-F10 cells at approximately 80% confluency and >90% viability were prepared for injection. For subcutaneous (s.c.) tumors, mice were injected with 4 x 10^5 KPC. 4662 cells or 5 × 10^5 B16-F10 cells on days 0 and 2 on the right and left flanks, respectively. Cells were injected in 100 μl DMEM or, for B16-F10, 50% growth factor-reduced Matrigel (BD). For orthotopic tumors, mice were injected with 1.25 × 10^5 KPC.4662 cells in 25μl of DMEM.

Orthotopic model

A transverse 10mm laparotomy incision was made in anesthetized mice and KPC.4662 cells were injected into the thickest portion of the pancreas. Visual blebbing confirmed successful implantation. Tumor cells were injected with 2μL of lipiodol (Guerbet; gift from Gregory Nadolskim and Michael Soulen, University of Pennsylvania), an oil-based, radioopaque contrast agent that allowed for tumor site visualization via CT. Flow cytometric analysis of tumor immune infiltrate confirmed that lipiodol had no immunomodulatory properties. Following tumor cell injection, a cotton swab was placed over the injection site for 1 minute to limit cell leakage into the peritoneal cavity. Gross dissection of the peritoneum 16 days after tumor injection showed intact pancreatic tumors with no peritoneal studding.

Disintegrating Polymend MT 5–0 sutures were used to perform a double layer closure of the peritoneal cavity and epidermal layer. Mice were monitored after surgery and given a dose of 0.1 mg/kg Buprenorphine SR (ZooPharm) i.p. every 4–6 hours for 72 hours.

KrasLSL^{G12D}-Trp53LSL^{R172H}-Pdx1-Cre model

KPC mice were evaluated for spontaneous tumor development via ultrasound every week using a Vevo 2100 Imaging System with 55 MHz MicroScan Transducer (Visual Sonics). Mice with tumors ≥30mm^3 were enrolled within 24 hr of baseline imaging using blocked randomization, and tumors were visualized for RT via laparotomy and lipiodol injection as described for the orthotopic model. Mice were designated as responders if tumor progression was <25% compared to baseline 14 days after initiation of therapy.

Tumor measurements

Electronic calipers were used to measure s.c. tumor diameter. Tumor volumes were calculated as: (length * width^2 * 0.52). Length was defined as the longest dimension and width was defined as perpendicular to length. Orthotopic pancreatic tumors were measured every two weeks using a Vevo 2100 Imaging System with 55 MHz MicroScan Transducer (Visual Sonics). Contours were drawn on tumor images to calculate tumor volumes using Visual Sonics software.

Radiation therapy

All radiotherapy was delivered using the Small Animal Radiation Research Platform (SARRP) (XStrahl) as previously described (19). A dose of 20 Gy was directly targeted to the tumor using a 0.5 cm^2 collimator rotated along a 180-degree arc during delivery to minimize exposure of surrounding normal tissue.

In vivo antibodies

In vivo antibodies were injected i.p. at 200 μg per dose, with the exception of αCD40 that was administered at 100 μg per dose and include: αCD4 (GK1.5), αCD40 (FGK4.5), αCD8 (2.43), αCTLA-4 (9H10), αLy6C (Monts 1), αIFNAR-1 (MAR1-5A3), αPD-1 (RMP1-14), and αIgG2A control (2A3). αCTLA-4 and αPD-1 were administered on days 5, 8, and 11 post-tumor injection. αCD40 was administered on day 11. αIFNAR-1. αCD4, and αCD8 were administered on days −2, 0, and every 3 days thereafter. αLy6C was administered on days 5, 6, 8, 11, and 13. All *in vivo* antibodies were purchased from Bio X Cell and verified to be endotoxin free.

Flow cytometry

Flow cytometric studies were performed on tumors, tumor draining lymph nodes, and spleen. Tumor, spleen, and lymph node single cell suspensions were prepared by mechanical dissociation through a 70μM cell strainer. Prior to mechanical dissociation, pancreatic tumors were incubated for 45 minutes in 1 mg/mL collagenase V in Dulbecco's Modified Eagle Medium (Thermo Fisher Scientific) at 37°C and spleen samples were incubated in ACK lysis buffer (Life Technologies) for three minutes. Single cell suspensions were then washed twice with PBS and enumerated (Beckman Coulter Counter Z2) before preparation

for analysis. Cell surface staining for flow cytometry was performed for 30 minutes in PBS with 2% FBS, and intracellular staining was performed using a fixation/permeabilization kit (eBioscience) according to the manufacturer's instructions. Live cells were identified using a Live/Dead Fixable Dead Cell Stain Kit (Life Technologies). Samples were run on a LSRII flow cytometer (BD). Cell number was calculated as: (tissue cell number * precent live cells/ tissue grams)

Histopathology

For histopathological analysis, tissues were fixed in zinc formalin, embedded in paraffin and 4–5 uM sections were stained with the following primary antibodies: mCD8a (Dianova DIA-808, 1:200) and SMA (Abcam ab5394, 1:200). Staining was performed on a Bond Max automated staining system (Leica Biosystems) using the Bond Intense R staining kit (Leica Biosystems DS9263.) The standard protocol was followed with the following exceptions: primary antibody incubation was extended to 1 hour at room temperature and Avidin Biotin Blocking (Vector Labs SP-2001) and Peptide Blocking (DAKO X0909) were added. Antigen retrieval was performed with E2 (mCD8a) or E1 (SMA) retrieval solution (Leica Biosystems) for 20 min. Sections were stained with the following secondary antibodies: biotinylated anti-rat (mCD8a, Vector BA-4001, 1:200) or anti-rabbit (SMA, Vector BA-1000, 1:200.) After staining, slides were rinsed, dehydrated through a series of ascending concentrations of ethanol and xylene, then coverslipped. For SMA score, the percentages of stromal cells positive for SMA was quantified in five fields under low magnification (×100). Staining intensity was graded on a scale of 0–3 compared with the total stromal area with 0 indicating 0%, 1 indicating ≤33%, 2 indicating 33%–66%, and 3 indicating > 66%.

Quantification and statistical analysis

Sample size—Sample sizes were estimated based on pilot experiments. Control mice were estimated to have an average tumor volume of $0.4cm^3$ at day 18. Treated mice were assumed to have 50% less average tumor volume when compared to control mice. Sigma was estimated to be 1.5. Using a 0.80 power at the 0.05 alpha level, we chose a sample size of 5 mice. Mice were randomly assigned a treatment or control group. For experiments where the treatment effect was expected to be small and/or weak, two independent researchers with one blinded to the treatment groups performed caliper tumor measurements.

Tumor kinetics—Differences in tumor growth were determined by a linear mixed-effects model using the *lmerTest* (version 2.0–33) and *lsmeans* (least-squares means method, version 2.26–3) R packages. R (https://www.r-project.org) was version 3.4.2. For plots of mean tumor size by treatment group, time points across experiments that differed by less than 48 hours were pooled. To avoid bias from dropout, time points were not graphed if the number of mice remaining alive was ≤65% of the maximum group size. Statistical analysis was performed using all data and correction for multiple comparisons was performed by calculating the false discovery rate (Benjamini & Hochberg, R version 3.4.3)

Random forest analysis—Random forest analysis is a multivariable non-parametric ensemble partitioning tree method for modeling classification, regression, or survival

problems (25,26), and was performed as previously described (19). This machine learning approach is used to determine how well input variables predict a response variable of interest. During bootstrapping, two-thirds of samples were used to train each tree and remaining (out-of-bag, OOB) samples were used for cross-validation and forest-related estimates. Missing values were imputed and the following tuning parameters were used: ntree = 3000; nodesize = 2; nsplit = 10; mtry = (input variable number$^{3/4}$). A Gini index splitting rule was used for classification and no iterative training or parameter optimization was performed.

Variables were then ranked by minimal depth (MD), a dimensionless statistic that measures variable predictiveness in tree-based models (27). For a variable *x*, MD is the shortest distance between the root node of a tree and the parent node of a maximal subtree. A maximal subtree is the largest subtree whose root node splits on *x*. Smaller MD values indicate greater predictiveness, *i.e.* greater importance to the overall ability of the model to correctly classify OOB samples.

Overall model performance was determined using OOB sample classification accuracy. Relative stability was determined using the normalized Brier score. Each analysis was externally cross-validated over 50 iterations using re-sampling without replacement (28). Overall accuracy, geometric mean accuracy and input variable MD was then compared to bootstrapped control data containing a scrambled response variable and significance was determined via FDR generated by Student's t-test or ANOVA with Tukey's HSD. All control data with scrambled response variables were non-predictive.

Kaplan-Meier survival analysis—Survival was recorded as the number of days from tumor injection until an event. An event was defined as tumor related death or euthanasia due to protocol-specified tumor burden. Overall p-values were calculated using the log-rank test (*survival* R package, version 2.42-0) and post-hoc testing was performed using the *survMisc* (*Pairwise survdiff* method) R package (version 0.5.4). Analyses were performed on all data. Correction for multiple comparisons was performed by calculating the false discovery rate (Benjamini & Hochberg).

Additional analysis software—Flow cytometric data were gated using FlowJo (version 10.3). The following R packages were used: cowplot (https://CRAN.R-project.org/package=cowplot, version 0.6.3): figure layouts, data.table (http://r-datatable.com, version 1.9.6): tabular data analysis, ggplot2 (version 2.1.0): general plots, pheatmap (https://CRAN.R-project.org/package=pheatmap, version 1.0.8): heatmaps, stats (version 3.3.2): tests for significance.

RESULTS

Radiotherapy and αCD40 override PDA resistance to αCTLA-4/αPD-1 immune checkpoint blockade

To determine the ability of radiotherapy (RT), αCD40 agonist mAb, and αCTLA-4/αPD-1 immune checkpoint blockade (ICB) (designated "RCP4") to mediate anti-tumor responses in PDA, we used a "two-tumor" s.c. KPC.4662 tumor model as previously described (Figure

1A) (19). Briefly, KPC.4662 cells were injected into both flanks and tumor-bearing mice were treated with *in vivo* antibodies i.p and/or 20 Gy radiation to only one tumor (the irradiated tumor).

We found that RT alone (designated "R") or in combination with ICB (designated "RCP") +/− αCD40 (RCP4) resulted in reduction of irradiated tumor growth, with 91% of RT-treated mice across groups achieving complete regression at this tumor site (Figure 1B). However, RT alone (R) or in combination with ICB (RCP) did not affect the growth of the unirradiated tumor or survival in these treatment groups (Figures 1C–D, Supplemental figure 1A). The addition of αCD40 to ICB (CP4) decreased growth of both the irradiated and unirradiated tumors and the effect was greatest when it was combined with both RT and ICB (RCP4) (Figures 1B–C, Supplemental figure 1A). Rates of long-term survival mirrored these observations: 0% in control mice compared to 17%, 50%, and 70% of mice treated with RCP, CP4, and RCP4, respectively (Figure 1D). Combination therapy with RCP4 resulted in protective immunity upon re-challenge with bilateral KPC.4662 tumors in 9/10 RCP4-treated mice (Figure 1E). In contrast, the addition of αCD40 to RT and ICB did not improve response in mice challenged with B16-F10 melanoma cells following the same experimental approach (Supplemental figure 1B–D). Thus, RCP4 augments anti-tumor immunity in ICB-refractory PDA, eradicating both index and unirradiated tumors in a majority of mice. αCD40 agonist mAb sensitizes the immune response to RT and ICB in PDA in a tumor specific fashion.

T and myeloid cells distinctly contribute to anti-tumor immunity

We next hypothesized that the RCP4 mediated anti-tumor immune response is T cell-dependent. To assess this hypothesis, T cells were depleted with αCD4 and/or αCD8 and tumor-bearing mice were treated with RCP4. Both CD4 and CD8 T cell depletion abrogated response to RCP4, resulting in greater unirradiated tumor burden and worse survival (Figure 2A–B). However, we noted that an initial tumor growth stabilization still occurred despite T cell depletion suggesting a potential T-cell independent mechanism of response (Supplemental figure 2A).

To assess the hypothesis that myeloid cells were required for the T-cell independent tumor regression we observed after RCP4, we evaluated response in mice lacking the long non-coding RNA (lncRNA) myeloid RNA regulator of Bim-induced death (*Morrbid*.) *Morrbid* is required for survival of short-lived myeloid cells via regulation of the pro-apoptotic gene *Bcl2l11* (29). Mice lacking *Morrbid* have greatly reduced populations of neutrophils, eosinophils, and Ly6C^{hi} myeloid cells, but normal numbers of other myeloid and lymphoid populations (29). *Morrbid*-knockout mice challenged with tumor and treated with RCP4 exhibited rapid growth in the unirradiated tumor with complete loss of response to therapy (Figure 2C, Supplemental figure 2B), and no survival advantage (Figure 2D). Consistent with this finding, addition of αLy6C depleting antibody (30) to RCP4 also negatively impacted survival due to unirradiated tumor outgrowth occurring after day 20 (Figure 2E–F, Supplemental figure 2C). Concomitant αLy6C and αCD4/αCD8 administration completely abrogated the RCP4 anti-tumor response. Thus, CD4 and CD8 T cells as well as *Morrbid*-

dependent short-lived myeloid cells cooperate for optimal response to combination RT, ICB and αCD40.

Response is dependent on CD40, IFNγ, and Batf3 but bypasses canonical activation pathways

To investigate host-dependent mediators of response to RCP4, we treated tumor-bearing CD40-knockout mice, IFNγ-knockout mice, and Batf3-knockout (which lack cross-presenting $CD8\alpha^+$ dendritic cells). Anti-tumor response and long-term survival were abrogated in CD40 and IFNγ-knockout mice (Figure 3A–B and Supplemental figure 2D). In Batf3-knockout mice, tumors initially responded to RCP4 treatment; however, this was not sustained past day 22 and there was no effect on overall survival. Given the requirement of CD40 for B cell responses (31), we also investigated if response to RCP4 is B cell-dependent. In mice lacking immunoglobulin heavy constant gamma 1 (μMT), or in mice lacking B cell activation factor and thus mature $B220^+$ B cells ($Tnfsf13b^{tm1Msc}$), we observed RCP4-mediated anti-tumor responses and overall survival that matched RCP4-treated wildtype mice (Supplemental figure 2E–2F). Thus, B cells do not appear to be required.

We next assessed if canonical innate activation pathways were required for response to RCP4, evaluating TLR4/MyD88, stimulator of interferon genes (STING) and interferon-α/interferon-β which have been shown to be critical for anti-tumor immunity (32–34). We found that mice lacking these pathways had fully intact anti-tumor immunity and survival (Supplemental figure 3A–D). Mice treated with IFNAR-blocking antibody, to exclude the possibility of cancer cell-autonomous type I interferon signaling, also showed no deficits in response. Thus, RCP4 anti-tumor immunity is dependent on host CD40, Batf3, and IFNγ, and is independent of B cells and canonical innate immune activation pathways.

Non-redundant immune contributions of radiotherapy, ICB, and CD40 to anti-tumor response

We investigated the myeloid and T cell compartments during the time course of RCP4 treatment to understand the contribution of each therapeutic component. To identify important immune metrics, we used random forest machine learning as previously described (19,36). Random forest is a multivariable, non-parametric ensemble partitioning tree method applicable to classification problems (25). We used RF to assess immune measurements in tumor, tumor-draining lymph node (TDLN), and spleen at 24h, 72h, and one week post-RT, which allowed us to model the effect of immune metrics over multiple treatment conditions and time points. We measured 23 immune markers across these permutations, resulting in more than 1,000 measurements. First, we determined if immune metrics could jointly classify mice into treatment groups with high accuracy. Second, we determined which immune metrics were most important to classification. Advantages of this approach compared to other methods are a lack of supervision; excellent discriminatory ability in high dimensional space; and resistance to noisy or interrelated input variables, missing data, and over-fitting.

Random forest analysis demonstrated that the effect of RT is best modeled 24h-post RT in TDLN and the irradiated tumor (Figure 4A–B). In TDLN, the top predictors of RT response were increased MHC class I/CD86 by percentage or median fluorescence intensity (MFI) principally on DEC205^{+} dendritic cells (Figure 4A, top, and Supplemental figure 4). Changes in total T and myeloid TDLN populations were not predictive (Figure 4A, bottom). Within the irradiated tumor, increased intratumoral CD11b^{+} myeloid cells and decreased total and CD8^{+}, but not CD4^{+}, T cells were predictive (Figure 4B, top vs. bottom and Supplemental figure 4). In both TDLN and irradiated tumor, total CD11c^{+} APCs were decreased after RT in most mice. These effects of RT were confined to the irradiated tumor and corresponding TDLN at 24h post-RT with no difference at 72h post-RT at these sites. No immune metrics could distinguish CP4 compared to RCP4 in the unirradiated tumor at any time point (overall model accuracy ≤60%, data not shown).

We next modeled the effect of αCD40 in the context of RT and ICB at peak tumor regression (i.e. one week post-RT), detecting substantial systemic and intratumoral immune reorganization due to αCD40 (Figure 4C–D). Systemically, a shift in splenic myeloid cells predictive of αCD40 consisted of decreased Ly6C^{hi} and F4/80^{+} myeloid cells (Figure 4C, top, and Supplemental figure 5). Decreased splenic total CD3 T cells were also a top predictor, with no predictive changes in proportion of CD4 or CD8 T cells (Figure 4C, bottom). The most predictive immune metrics in the tumor were decreases in CD4^{-}CD8^{-} T cells, CD49b^{+} non-T cells, and regulatory T cells, and increases in CD11c^{+} APCs and total T cells (Figure 4D, top, and Supplemental figure 5). Similar to the spleen, the intratumoral ratio of CD4 to CD8 T cells was unaffected (Figure 4D, bottom).

Random forest analysis further revealed that the addition of ICB and αCD40 to RT could be predicted by favorable recomposition of the T cell compartment at peak tumor regression one week post-RT in the unirradiated tumor (Figure 4E). Most predictive was an increase in intratumoral CD8 T cells, expressed as either a proportion of all CD45^{+} leukocytes or CD3 T cells (Figure 4E, top and Supplemental figure 6). In addition, there is a corresponding decreased proportion of CD4^{-}CD8^{-} T cells as well as increased CD11b^{-}Gr1^{+} myeloid cells, whereas changes in total CD4 T cells, CD11b^{+} myeloid, or CD11c^{+} APCs were not predictive (Figure 4E, bottom).

Our unbiased assessment of immune changes following RCP4 compared to control mice surprisingly revealed that a decrease in intratumoral CD4^{-}CD8^{-} T cells was the single best predictor of whether mice received therapy (Figure 4F, top and Supplemental figure 6). Together with a corresponding increase in CD8 T cells and CD8/regulatory T cell ratio in the unirradiated tumor, 90% of RCP4-treated mice are correctly classified one week post-RT. Reduced prevalence of CD11c^{+} APCs and regulatory T cells as a percentage of all T cells were also top predictors. Furthermore, at one week post-RT no other alterations in intratumoral myeloid subsets were predictive (Figure 4F, bottom). When we evaluated immune changes in RCP4-treated mice over time, we observed reduced intratumoral APCs and increased T cells, mirroring predictive changes between control and RCP4-treated mice (Supplemental figure 7A–B). In summary, RT triggers an early proinflammatory stimulus-ablating existing CD8 T cells and upregulating antigen presentation machinery in the irradiated tumor and TDLN 24h post-RT. At peak tumor regression, αCD40 causes systemic

myeloid compartment reorganization that is identified in both the tumor and spleen, while ICB increases intratumoral T cell infiltration, thereby improving the CD8/regulatory T cell ratio.

Combination therapy attenuates growth of orthotopic and *de novo* PDA tumors

To determine if anatomic location impacts response, we also investigated RCP4 in orthotopic and *de novo* KPC PDA models. The KPC model manifests some of the hallmarks of human PDA such as minimal non-synonymous mutations, dense desmoplasia, recruitment of tumor-promoting myeloid and regulatory T cells, and minimal CD8 T cell infiltrate (10,23). Briefly, mice bearing a single orthotopic pancreatic tumor (surgically injected or spontaneous in the orthotopic and KPC models, respectively) were treated with ICB, αCD40, and/or RT as per the regimen previously described in Figure 1A and tumor volume was documented using ultrasound. In the orthotopic model, αCD40 in combination with ICB (CP4) decreased tumor growth (Figure 5A) and increased overall survival (Figure 5B) in comparison to control. However, the greatest response occurred with the addition of RT to ICB and αCD40 (RCP4), which resulted in a significant reduction in tumor burden (Figure 5A) and improvement in overall survival (Figure 5B) in comparison to both control and CP4 treated mice. Treatment was durable, generating protective immunity to s.c. rechallenge in 5/6 RCP4-treated mice with initial complete responses (Figure 5C). Thus, RCP4 generates potent antitumor immunity in the pancreas, and RT and aCD40 are required to maximize response.

We next assessed response in the *de novo* KPC model, finding that RCP4 resulted in significant inhibition of tumor growth compared to control mice (Figure 5D). Two weeks after treatment with RCP4, we observed stable disease in 7/29 KPC mice treated with RCP4 (24%), compared to 0/22 control mice. Thus, at the primary site of disease in the pancreas, RCP4 results in higher rates of complete response in the orthotopic model and reduced tumor growth in the *de novo* KPC tumors.

Though there were significant responses in both the orthotopic and *de novo* KPC models, they were not as robust as those in the subcutaneous model. To identify possible causes, we examined intratumoral CD8 T cells and stroma in both untreated controls and RCP4 treated mice. There were significantly more infiltrating CD8 T cells in the untreated controls in the subcutaneous model in comparison to the orthotopic and KPC models (Supplemental figure 8A). With RCP4 treatment, the number of infiltrating CD8 T cells significantly increased in subcutaneous and orthotopic tumors, but the response was less robust in KPC tumors. There were comparable levels of SMA in all untreated control tumors, which decreased proportionally with RCP4 treatment (Supplemental figure 8B.)

DISCUSSION

PDA remains refractory to conventional and immune approaches, with combination chemotherapy only modestly improving survival (3,8,9,37). Here, using genetically engineered mouse models of PDA that recapitulate this clinical challenge, we demonstrate that the combination of RT, ICB, and αCD40 generate potent anti-tumor T cell immunity. Although effective in other models, combination RT and ICB was insufficient in PDA. We

found here that αCD40 was critical to achieving an anti-tumor effect, but the greatest benefit occurred with the combination of ICB, RT and αCD40. Using random forest immune analysis, we found that (i) αCD40 uniquely reorganizes and activates the myeloid and APC compartment, (ii) RT non-redundantly ablates existing intratumoral T cells and upregulates MHC class I/CD86, and (iii) ICB increases the prevalence of intratumoral CD8 T cells (Supplemental figure 9.) Anti-tumor immunity was dependent on host CD40, Batf3, and IFNγ, and did not require innate immune activation pathways such as STING. Thus, our findings provide a rationale for the clinical evaluation of combination therapy with RT, ICB, and αCD40 in PDA.

RF immune analysis revealed that RT and aCD40 non-redundantly alter immune dynamics during response. In addition to upregulation of antigen presentation machinery, irradiated tumors became void of total T cells, especially CD8 T cells, 24 hours after irradiation, consistent with the high radiosensitivity of most T cells. In contrast, intratumoral CD8 T cells in the unirradiated tumor increased at peak tumor regression with RCP4. The early post-RT T cell depletion we observed - and the lack of any detectable immune signature for RT in unirradiated tumor after 72 hours - suggest that RT may modify adaptive immunity by “creating space” for an influx of cytolytic T cells. In contrast to local RT effects, in the context of RT and ICB, αCD40 resulted in dramatic fluctuation of $CD11b^+$ myeloid and $CD11c^+$ APC populations in tumor and spleen during peak tumor regression. Thus, RT and αCD40 have qualitatively and temporally distinct effects on innate and adaptive immune populations. Moreover, the effect of ICB was also unique, resulting in increased prevalence of intratumoral CD8 T cells, and combination RCP4 ultimately culminates in increased intratumoral CD8 T cell/regulatory T cell ratio during peak tumor regression.

CD40 agonism and ICB differ fundamentally in pharmacodynamic effects, but both are IFNγ dependent. αCD40 is well-described to activate multiple cell types that contribute to anti-tumor immunity, influencing the immune response proximal to T cell priming (31). We hypothesize that CD40 activation in combination with RT, chemotherapy, or vaccines may be able to trigger anti-tumor T cells in tumors otherwise immunologically “cold” and thereby sensitize for response to ICB. Both CD40 agonism and ICB are dependent on IFNγ; in the context of αCD40, IFNγ redirects inflammatory monocytes to secrete matrix metalloproteinases that digest PDA tumor ECM (38). Thus, IFNγ may be required for T cell infiltration into tumors in addition to myeloid cell-mediated anti-tumor activity, consistent with the dependency of RCP4 response on IFNγ that we observe.

Our results suggest that CD40 agonists may be able to reprogram Ly6C myeloid cells from tumor-promoting to tumor-suppressive. Previous work in KPC PDA has shown that RT can induce both immunosuppressive macrophages that inhibit T cells and $Ly6C^{hi}$ myeloid cells that promote neovascularization (39,40). Here, we show that in combination with RT and ICB, CD40 agonist response is dependent on the lncRNA myeloid regulator *Morrbid* and $Ly6C^{hi}$ myeloid cells. These findings suggest that RT-induced, tumor-promoting myeloid populations may be re-programmable via CD40 signaling. Furthermore, *Morrbid*-knockout mice can be used as a cell type-specific tool to investigate the complex role of myeloid cells in anti-tumor responses. We have previously demonstrated that αCD40 can induce tumor regression via macrophages when used as monotherapy and trigger T cell immunity when

used in combination with ICB and chemotherapy (20–22). The complete loss of RCP4 response in *Morrbid*-knockout mice suggests that short-lived myeloid cells may be critical for both myeloid and T cell-induced immunity with combination therapy.

Our unsupervised random forest immune analysis unexpectedly identified a decrease in intratumoral $CD4^{-}CD8^{-}$ T cells as the best predictor of whether mice received RCP4 compared to control. This finding provides a strong rationale for the use of unsupervised approaches in high dimensional immune analysis to reveal novel mechanistic insights. $CD4^{-}CD8^{-}$ T cells are likely to be γδ T cells, which may have an immunosuppressive role in PDA (41). γδ T cells are highly prevalent in PDA and promote pancreatic oncogenesis by inhibiting αβ T cells via immune checkpoint receptor ligation (41). Thus, reduction in prevalence of γδ T cells with RCP4 is consistent with RCP4 converting the tumor microenvironment from suppressive to stimulatory.

Overcoming immunosuppressive barriers in PDA is likely to require coordinated targeting of innate and adaptive immunity. We show here that RT and αCD40 are key links between these systems, ameliorating resistance to ICB in PDA via multiple cellular mechanisms. Clinical trials combining RT+αCD40 (NCT03165994) and αCD40+ICB (NCT03123783, NCT01103635, NCT02706353, NCT02304393, NCT03214250) are underway, including in PDA (38,42). Our results provide rationale for combining RT, αCD40, and ICB in human PDA.

Supplementary Material

Refer to Web version on PubMed Central for supplementary material.

Acknowledgments

This work was supported by the National Institutes of Health (NIH) (P01 CA210944 to A.J. Minn and R.H. Vonderheide; R01 CA169123 and P30 CA016520 to R.H. Vonderheide; R01CA172651 to A.J. Minn; R21AI128060, R21DK111755, and R01HL136572 to J. Henao-Mejia; and F30HL138739-01A1 to J.J. Kotzin), the Parker Institute for Cancer Immunotherapy (A.J. Rech, A.J. Minn, and R.H. Vonderheide), the American Gastroenterological Association (Research Scholar Award to C. Twyman-Saint Victor), the Robert Wood Johnson Foundation (Harold Amos Medical Faculty Development Program to C. Twyman-Saint Victor), and the PEW Charitable Trust (J. Henao-Mejia). We gratefully acknowledge K.T. Byrne, B. Z. Stanger, A. Maity, E.J. Wherry, C. Clendenin, and M. Liu for helpful discussions, and Lindsay Herman, the Abramson Cancer Center Pancreatic Cancer “Mouse Hospital”, Small Animal Imaging facility, and Small Animal Radiation Research Platform operators W.T. Jenkins and K. Shoniyozov for technical assistance. Immunohistochemical and special stains were performed at the Pathology Core Lab at the Children’s Hospital of Philadelphia Research Institute. Pathology analysis was done by Anirban Maitra and Jun Zhao at the MD Anderson Cancer Center.

References

1. Hodi FS, O’Day SJ, McDermott DF, Weber RW, Sosman JA, Haanen JB, et al. Improved survival with ipilimumab in patients with metastatic melanoma. N Engl J Med. 2010; 363:711–23. [PubMed: 20525992]
2. Hamid O, Robert C, Daud A, Hodi FS, Hwu W-J, Kefford R, et al. Safety and tumor responses with lambrolizumab (anti-PD-1) in melanoma. N Engl J Med. 2013; 369:134–44. [PubMed: 23724846]
3. Brahmer JR, Tykodi SS, Chow LQM, Hwu W-J, Topalian SL, Hwu P, et al. Safety and activity of anti-PD-L1 antibody in patients with advanced cancer. N Engl J Med. 2012; 366:2455–65. [PubMed: 22658128]

4. Royal RE, Levy C, Turner K, Mathur A, Hughes M, Kammula US, et al. Phase 2 trial of single agent Ipilimumab (anti-CTLA-4) for locally advanced or metastatic pancreatic adenocarcinoma. J Immunother. 2010; 33:828–33. [PubMed: 20842054]
5. Rahib L, Smith BD, Aizenberg R, Rosenzweig AB, Fleshman JM, Matrisian LM. Projecting cancer incidence and deaths to 2030: the unexpected burden of thyroid, liver, and pancreas cancers in the United States. Cancer Res. 2014; 74:2913–21. [PubMed: 24840647]
6. Siegel RL, Miller KD, Jemal A. Cancer statistics, 2016. CA Cancer J Clin. 2016; 66:7–30. [PubMed: 26742998]
7. Rhim AD, Mirek ET, Aiello NM, Maitra A, Bailey JM, McAllister F, et al. EMT and dissemination precede pancreatic tumor formation. Cell. 2012; 148:349–61. [PubMed: 22265420]
8. Von Hoff DD, Ervin T, Arena FP, Chiorean EG, Infante J, Moore M, et al. Increased survival in pancreatic cancer with nab-paclitaxel plus gemcitabine. N Engl J Med. 2013; 369:1691–703. [PubMed: 24131140]
9. Conroy T, Desseigne F, Ychou M, Bouché O, Guimbaud R, Bécouarn Y, et al. FOLFIRINOX versus gemcitabine for metastatic pancreatic cancer. N Engl J Med. 2011; 364:1817–25. [PubMed: 21561347]
10. Clark CE, Hingorani SR, Mick R, Combs C, Tuveson DA, Vonderheide RH. Dynamics of the immune reaction to pancreatic cancer from inception to invasion. Cancer Res. 2007; 67:9518–27. [PubMed: 17909062]
11. Hruban RH, Klimstra DS. Adenocarcinoma of the pancreas. Semin Diagn Pathol. 2014; 31:443–51. [PubMed: 25441308]
12. Fukunaga A, Miyamoto M, Cho Y, Murakami S, Kawarada Y, Oshikiri T, et al. CD8+ tumor-infiltrating lymphocytes together with CD4+ tumor-infiltrating lymphocytes and dendritic cells improve the prognosis of patients with pancreatic adenocarcinoma. Pancreas. 2004; 28:e26–31. [PubMed: 14707745]
13. Vonderheide RH, Bayne LJ. Inflammatory networks and immune surveillance of pancreatic carcinoma. Curr Opin Immunol. 2013; 25:200–5. [PubMed: 23422836]
14. Feig C, Jones JO, Kraman M, Wells RJB, Deonarine A, Chan DS, et al. Targeting CXCL12 from FAP-expressing carcinoma-associated fibroblasts synergizes with anti-PD-L1 immunotherapy in pancreatic cancer. Proc Natl Acad Sci USA. 2013; 110:20212–7. [PubMed: 24277834]
15. Balli D, Rech AJ, Stanger BZ, Vonderheide RH. Immune cytolytic activity stratifies molecular subsets of human pancreatic cancer. Clin Cancer Res. 2017; 23:3129–38. [PubMed: 28007776]
16. Ino Y, Yamazaki-Itoh R, Shimada K, Iwasaki M, Kosuge T, Kanai Y, et al. Immune cell infiltration as an indicator of the immune microenvironment of pancreatic cancer. Br J Cancer. 2013; 108:914–23. [PubMed: 23385730]
17. Farren MR, Mace TA, Geyer S, Mikhail S, Wu C, Ciombor K, et al. Systemic immune activity predicts overall survival in treatment-naïve patients with metastatic pancreatic cancer. Clin Cancer Res. 2016; 22:2565–74. [PubMed: 26719427]
18. Shabason JE, Minn AJ. Radiation and immune checkpoint blockade: from bench to clinic. Semin Radiat Oncol. 2017; 27:289–98. [PubMed: 28577836]
19. Twyman-Saint Victor C, Rech AJ, Maity A, Rengan R, Pauken KE, Stelekati E, et al. Radiation and dual checkpoint blockade activate non-redundant immune mechanisms in cancer. Nature. 2015; 520:373–7. [PubMed: 25754329]
20. Beatty GL, Chiorean EG, Fishman MP, Saboury B, Teitelbaum UR, Sun W, et al. CD40 agonists alter tumor stroma and show efficacy against pancreatic carcinoma in mice and humans. Science. 2011; 331:1612–6. [PubMed: 21436454]
21. Byrne KT, Vonderheide RH. CD40 stimulation obviates innate sensors and drives T cell immunity in cancer. CellReports. 2016; 15:2719–32.
22. Winograd R, Byrne KT, Evans RA, Odorizzi PM, Meyer ARL, Bajor DL, et al. Induction of T-cell immunity overcomes complete resistance to PD-1 and CTLA-4 blockade and improves survival in pancreatic carcinoma. Cancer Immunol Res. 2015; 3:399–411. [PubMed: 25678581]
23. Hingorani SR, Wang L, Multani AS, Combs C, Deramaudt TB, Hruban RH, et al. Trp53R172H and KrasG12D cooperate to promote chromosomal instability and widely metastatic pancreatic ductal adenocarcinoma in mice. Cancer Cell. 2005; 7:15–5.

24. Bayne LJ, Beatty GL, Jhala N, Clark CE, Rhim AD, Stanger BZ, et al. Tumor-derived granulocyte-macrophage colony-stimulating factor regulates myeloid inflammation and T cell immunity in pancreatic cancer. Cancer Cell. 2012; 21:822–35. [PubMed: 22698406]
25. Breiman L. Random Forests. Statistics Department, University of California. Machine Learning. 2001; 45:5–32.
26. Chen X, Ishwaran H. Random forests for genomic data analysis. Genomics. 2012; 99:323–9. [PubMed: 22546560]
27. Ishwaran H, Kogalur UB, Gorodeski EZ, Minn AJ, Lauer MS. High-dimensional variable selection for survival data. J Am Stat Assoc. 2010; 105:205–17.
28. Strobl C, Boulesteix A-L, Kneib T, Augustin T, Zeileis A. Conditional variable importance for random forests. BMC Bioinformatics. 2008; 9:307. [PubMed: 18620558]
29. Kotzin JJ, Spencer SP, McCright SJ, Kumar DBU, Collet MA, Mowel WK, et al. The long non-coding RNA Morrbid regulates Bim and short-lived myeloid cell lifespan. Nature. 2016; 537:239–43. [PubMed: 27525555]
30. Rowe AM, Yun H, Treat BR, Kinchington PR, Hendricks RL. Subclinical Herpes simplex virus type 1 infections provide site-specific resistance to an unrelated pathogen. J Immunol. 2017; 198:1706–17. [PubMed: 28062697]
31. Vonderheide RH, Glennie MJ. Agonistic CD40 antibodies and cancer therapy. Clin Cancer Res. 2013; 19:1035–43. [PubMed: 23460534]
32. Ahonen CL, Wasiuk A, Fuse S, Turk MJ, Ernstoff MS, Suriawinata AA, et al. Enhanced efficacy and reduced toxicity of multifactorial adjuvants compared with unitary adjuvants as cancer vaccines. Blood. 2008; 111:3116–25. [PubMed: 18202224]
33. Deng L, Liang H, Xu M, Yang X, Burnette B, Arina A, et al. STING-dependent cytosolic DNA sensing promotes radiation-induced type I interferon-dependent antitumor immunity in immunogenic tumors. Immunity. 2014; 41:843–52. [PubMed: 25517616]
34. Burnette BC, Liang H, Lee Y, Chlewicki L, Khodarev NN, Weichselbaum RR, et al. The efficacy of radiotherapy relies upon induction of type i interferon-dependent innate and adaptive immunity. Cancer Res. 2011; 71:2488–96. [PubMed: 21300764]
35. Woo S-R, Fuertes MB, Corrales L, Spranger S, Furdyna MJ, Leung MYK, et al. STING-dependent cytosolic DNA sensing mediates innate immune recognition of immunogenic tumors. Immunity. 2014; 41:830–42. [PubMed: 25517615]
36. Ishwaran H, Gerds TA, Kogalur UB, Moore RD, Gange SJ, Lau BM. Random survival forests for competing risks. Biostatistics. 2014; 15:757–73. [PubMed: 24728979]
37. Herbst RS, Soria J-C, Kowanetz M, Fine GD, Hamid O, Gordon MS, et al. Predictive correlates of response to the anti-PD-L1 antibody MPDL3280A in cancer patients. Nature. 2014; 515:563–7. [PubMed: 25428504]
38. Long KB, Gladney WL, Tooker GM, Graham K, Fraietta JA, Beatty GL. IFNγ and CCL2 cooperate to redirect tumor-infiltrating monocytes to degrade fibrosis and enhance chemotherapy efficacy in pancreatic carcinoma. Cancer discovery. 2016; 6:400–13. [PubMed: 26896096]
39. Seifert L, Werba G, Tiwari S, Giao Ly NN, Nguy S, Alothman S, et al. Radiation therapy induces macrophages to suppress T-cell responses against pancreatic tumors in mice. Gastroenterology. 2016; 150:1659–1672e5. [PubMed: 26946344]
40. Kalbasi A, Komar C, Tooker GM, Liu M, Lee JW, Gladney WL, et al. Tumor-derived CCL2 mediates resistance to radiotherapy in pancreatic ductal adenocarcinoma. Clin Cancer Res. 2017; 23:137–48. [PubMed: 27354473]
41. Daley D, Zambirinis CP, Seifert L, Akkad N, Mohan N, Werba G, et al. Gammadelta T cells support pancreatic oncogenesis by restraining alphabeta T cell activation. Cell. 2016; 166:1485–1499e15. [PubMed: 27569912]
42. Sharabi AB, Lim M, DeWeese TL, Drake CG. Radiation and checkpoint blockade immunotherapy: radiosensitisation and potential mechanisms of synergy. Lancet Oncol. 2015; 16:e498–509. [PubMed: 26433823]

Significance

Radiotherapy and αCD40 disrupt key links between innate and adaptive immunity, ameliorating resistance to immune checkpoint blockade in pancreatic cancer via multiple cellular mechanisms.

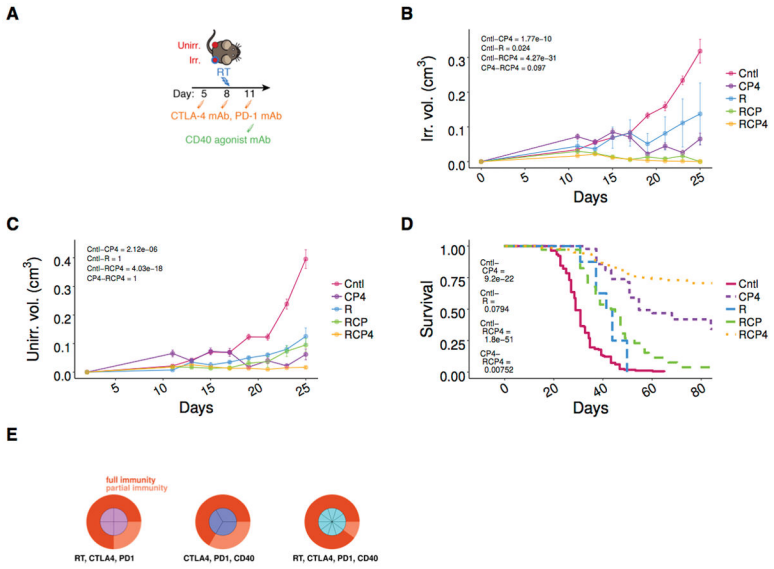

Figure 1. Radiotherapy, αCD40 override resistance to αCTLA-4/αPD-1 immune checkpoint blockade in PDA

A. Experimental design. Mice were injected s.c. on each flank on days 0 and 2 with KPC.4662 PDA cells followed by treatment with radiotherapy (RT), αCD40, and/or ICB (αCTLA-4 and αPD-1). 20 Gy RT was delivered on day 8 to the right-sided tumor (irradiated tumor), ICB was administered on days 5, 8, and 11, and αCD40 was administered on day 11. **B–C**. Mean growth kinetics of irradiated (*B*) and unirradiated (*C*) tumor following treatment. **D.** Overall survival. Data are from 2–6 independent experiments each with 5–10 mice/group. Growth curves represent mean ± *s.e.m.* Significance was determined via mixed linear effect model followed by least-squares means (B, C) or Log-Rank (D) and is corrected for multiple comparisons. **E.** Mice with no evidence of disease were rechallenged with KPC.4662 PDA cells on both flanks 75–100 days after initial tumor injection. The outcome of rechallenge (either full immunity (i.e. no tumor) or partial immunity (i.e. delayed tumor growth)) are shown per initial treatment.

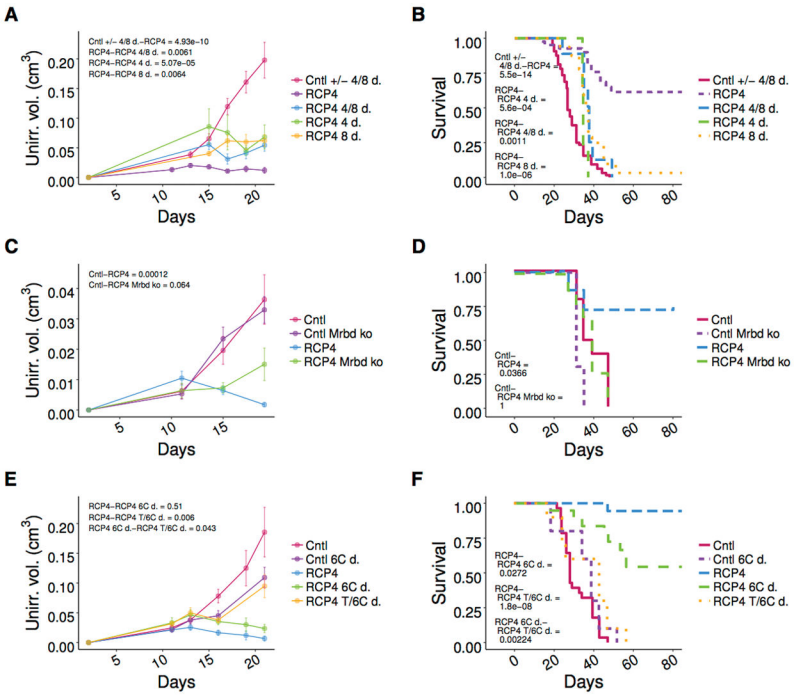

Figure 2. T and myeloid cells contribute distinctly to anti-tumor immunity

A–B. T cell depleting antibodies were administered every three days beginning on day -2 and mice treated as in Figure 1A. Shown is the mean growth kinetics of the unirradiated tumor *(A)* and corresponding survival *(B)*. **C–D.** *Morrbid* KO mice treated as in Figure 1A. Shown is mean growth kinetics of the unirradiated tumor *(C)* and corresponding survival *(D)*. **E–F.** Ly6C depleting antibody was administered on days 5, 6, 8, 11, and 13 and mice treated as in Figure 1A. Shown is the mean growth kinetics of the unirradiated tumor *(E)* and corresponding survival *(F)*. *4 d.*= CD4 T cell depletion; *8 d.*= CD8 T cell depletion; *4 d./8 d.*= CD4 + CD8 T cell depletion; *6C d.* = Ly6C depletion; and *T/6C d.*= CD4 + CD8 T cell + Ly6C depletion. Data are from 2–4 independent experiments, each with 5–10 mice/group. Growth curves represent mean ± *s.e.m.* Significance was determined via mixed linear effect model followed by least-squares means (A, C, E) or Log-Rank (B, D, F) and is corrected for multiple comparisons.

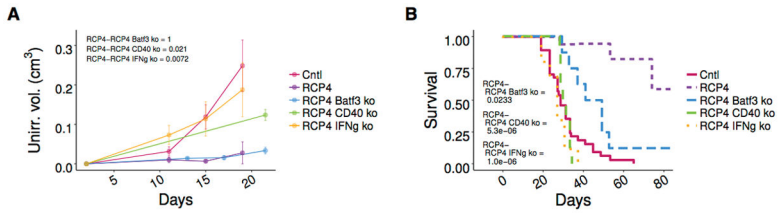

Figure 3. Radiotherapy, ICB, αCD40 PDA response is dependent on CD40, Batf3, and IFNγ

A–B. Batf3 KO, CD40 KO or IFNγ KO mice were treated as per Figure 1A. Shown is the mean growth kinetics of the unirradiated tumor *(A)* and corresponding survival *(B)*. Growth curves represent mean ± *s.e.m.* No differences in tumor kinetics or survival existed between untreated mice (WT and knockouts), thus all untreated mice were pooled for clarity (designated “Cntl”“). Significance was determined via mixed linear effect model followed by least-squares means (A) or Log-Rank (B) and is corrected for multiple comparisons.

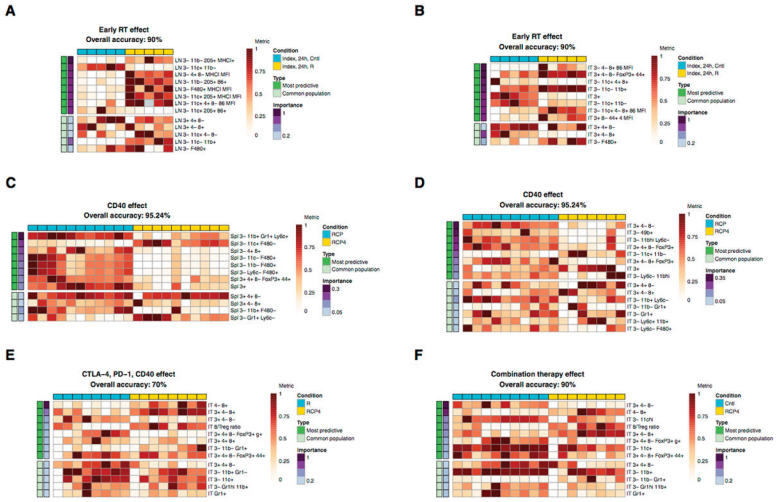

Figure 4. Radiotherapy, ICB, αCD40 non-redundantly modify tumor immune infiltrate

A–F. Random forest analysis (RF) of tumor infiltrate shows distinct component contributions to immunity. RF is a multivariable, non-parametric ensemble partitioning tree method for modeling classification. This approach is used to model the importance of flow cytometry metrics to classification by treatment group in an unsupervised, robust manner. Heatmaps show flow cytometry metrics normalized by row. Each box is an individual mouse. Rows are ordered from top to bottom by importance to RF model predictiveness, expressed as minimal depth distance from threshold (see *Materials and methods*). The top heatmap in each panel shows the most important metrics to classification and the bottom heatmap shows the importance of common immune metrics. Columns are hierarchically clustered within treatment groups. Mice were treated as described in Figure 1 and tissue was harvested and analyzed via flow cytometry. Phenotypes listed indicate the proportion of the parent population, grandparent population (g), or mean fluorescent intensity (MFI), pre-gated on live, $CD45^+$ cells unless otherwise indicated. *LN* = tumor-draining lymph node; *IT* = intratumoral immune infiltrate; *Spl* = spleen. **A–B.** RF model for radiotherapy compared to control 24 hours after RT in tumor-draining lymph node *(A)* and irradiated tumor *(B)*. **C–D.** RF model for addition αCD40 at peak tumor regression (1 week after radiotherapy) in spleen (*C*) and orthotopic tumor (*D*). **E.** RF model for addition of ICB and αCD40 at peak regression in the unirradiated tumor **F.** RF model for combination therapy with RT, αCD40, and ICB at peak unirradiated tumor regression. See Supplemental figure 7 for immune changes over time and Supplemental figures 4–6 for corresponding boxplots of flow cytometry metrics shown.

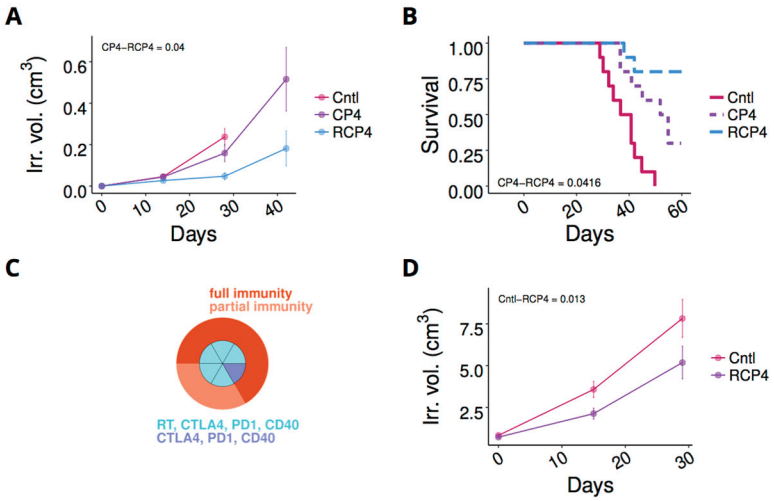

Figure 5. Radiotherapy, ICB, αCD40 improves response of orthotopic KPC.4662 and *de novo KPC* tumors

A–C. Mice were injected with a single KPC.4662 orthotopic pancreatic tumor on day 0 followed by treatment with ICB (days 6, 9 and 12) and αCD40 (day 12) ± 20 Gy RT (day 9). Shown is the mean tumor growth kinetics *(A)* and corresponding overall survival *(B)*. **C.** Mice with no evidence of disease were rechallenged with s.c. KPC.4662 PDA cells 75–100 days after initial tumor injection. The outcome of rechallenge (either full immunity (i.e. no tumor) or partial immunity (i.e. delayed tumor growth)) are shown per initial treatment. **D.** KPC mice with spontaneous tumors ≥30mm^3 were treated as in *(A)*. Shown is the mean tumor growth kinetics. Data are from 2 independent experiments, each having 5–10 mice/group. Tumor growth curves represent mean ± *s.e.m.* Significance was determined via mixed linear effect model followed by least-squares means (*A,D*) or Log-Rank (*B*) and is corrected for multiple comparisons.